Available online at www.sciencedirect.com
SCIENCE DIRECT®
Journal of Computational Physics 190 (2003) 523–549
JOURNAL OF COMPUTATIONAL PHYSICS
www.elsevier.com/locate/jcp

Spectral/*hp* least-squares finite element formulation for the Navier–Stokes equations

J.P. Pontaza *, J.N. Reddy

Department of Mechanical Engineering, Texas A&M University, College Station, TX 77843-3123, USA

Received 3 July 2002; received in revised form 24 February 2003; accepted 28 May 2003

Abstract

We consider the application of least-squares finite element models combined with spectral/*hp* methods for the numerical solution of viscous flow problems. The paper presents the formulation, validation, and application of a spectral/*hp* algorithm to the numerical solution of the Navier–Stokes equations governing two- and three-dimensional stationary incompressible and low-speed compressible flows. The Navier–Stokes equations are expressed as an equivalent set of first-order equations by introducing vorticity or velocity gradients as additional independent variables and the least-squares method is used to develop the finite element model. High-order element expansions are used to construct the discrete model. The discrete model thus obtained is linearized by Newton's method, resulting in a linear system of equations with a symmetric positive definite coefficient matrix that is solved in a fully coupled manner by a preconditioned conjugate gradient method. Spectral convergence of the L_2 least-squares functional and L_2 error norms is verified using smooth solutions to the two-dimensional stationary Poisson and incompressible Navier–Stokes equations. Numerical results for flow over a backward-facing step, steady flow past a circular cylinder, three-dimensional lid-driven cavity flow, and compressible buoyant flow inside a square enclosure are presented to demonstrate the predictive capability and robustness of the proposed formulation.

Keywords: Spectral methods; *hp* Methods; Least-squares; Incompressible flow; Low-speed compressible flow

1. Introduction

During the past three decades considerable efforts have been directed towards the development of robust computational procedures for fluid flow problems. However, in the context of fluid flow analyses, the finite element method has yet to achieve the same level of acceptance as other numerical methods, such as (low order) control-volume based methods. More recently, interest has shifted towards high-order accurate numerical solutions of the Navier–Stokes equations and its here that spectral/*hp* finite element formulations

* Corresponding author.
E-mail addresses: pontaza@tamu.edu (J.P. Pontaza), jnreddy@shakti.tamu.edu (J.N. Reddy).
URL: http://people.tamu.edu/~pontaza/.

0021-9991/$ - see front matter
doi:10.1016/S0021-9991(03)00296-1

have proven to be more efficient [1]. Encouraged by the success of spectral/*hp* methods in computational fluid dynamics, we wish to combine these ideas with least-squares variational principles, which offer many theoretical and computational advantages in the implementation of the corresponding finite element model that are not present in the weak form Galerkin finite element model.

It is well known that application of the weak form Galerkin procedure to problems whose solutions can be characterized as global minimizers results in global minimization of quadratic functionals, such is the case for linear elasticity problems; see [2]. In this case, given a conforming discretization, the finite element solution is an orthogonal projection of the exact solution onto the trial space, i.e., the finite element solution is a minimizer of an energy functional on the trial space so that it represents the best possible approximation in the energy norm. Such a setting, hereafter referred to as a *variational setting*, is the most favorable for a finite element approximation.

Failure to immediately recognize the link between global minimization of unconstrained convex functionals and the success of the method for linear elasticity problems led to early attempts to extend weak form Galerkin formulations beyond problems whose solutions could be characterized as unconstrained global minimizers. For example, problems of the saddle-point type, whose solution can be interpreted as a constrained minimization of a convex functional by requiring adherence of the discrete spaces to restrictive compatibility conditions; lack many of the attractive properties of the variational setting. Implementation of weak form Galerkin finite element models without accounting for the restrictive conditions leads to the occurrence of spurious oscillations in the numerical solution. A typical example is given by the primitive variable formulation of the Stokes problem for which the velocity and pressure approximation spaces cannot be chosen independently and must satisfy an inf–sup condition (see, e.g. [3]).

In the context of the Stokes and/or the Navier–Stokes equations, various finite element models attempting to fully or partially recover some of the properties of the variational setting have been proposed, and among them the Galerkin-least-squares and stabilized Galerkin methods have been extensively researched (see, e.g. [4,5]).

In the past few years finite element models based on least-squares variational principles have drawn considerable attention (see, e.g. [6,7]). In particular, given a partial differential equation or a set of partial differential equations, the least-squares method allows us to define a convex, unconstrained minimization principle so that a finite element model can be developed in a variational setting. Direct application of least-squares principles to develop finite element models for the Navier–Stokes equations requires that the piecewise polynomial functions be at least once continuously differentiable across element boundaries (C^1 continuity). Early implementations failed to gain popularity because of this requirement. In practical implementations of least-squares finite element models, the Navier–Stokes equations are transformed into an equivalent first-order system. This allows the use of nodal/modal expansions that are merely C^0 continuous across element boundaries.

For practical reasons, we use L_2-norms of the residuals of equations to define the least-squares functional. Moreover, we can require the boundary conditions to be imposed either strongly or, alternatively, in a weak sense through the least-squares functional. The latter will be exploited in the present study to treat outflow boundary conditions. In order to fully emulate the variational setting, one must define a L_2 least-squares functional that is H^1-norm equivalent [7]. If this is achieved, the least-squares finite element solution can be interpreted as an orthogonal projection in the Hilbert space with respect to problem dependent inner products, and stability requirements such as inf–sup conditions will never arise. A notable computational advantage of working in such a setting is that the resulting algebraic problem will have a symmetric positive definite (SPD) coefficient matrix, which can be solved by using robust iterative methods, such as preconditioned conjugate gradient methods.

Identifying norm equivalent functionals associated with a partial differential equation is not a trivial task. We rely on the Agmon, Douglis, and Nirenberg (ADN) theory [8] for elliptic operators to identify

appropriate spaces to define a least-squares functional that is norm-equivalent. First-order differential operators that are homogeneous elliptic in the ADN sense allow the construction of a L_2 least-squares functional that is H^1-norm equivalent. For non-homogeneous elliptic first-order differential operators (in the ADN sense), a norm-equivalent least-squares functional may also be constructed. However, the least-squares functional will be in terms of computationally impractical norms which must be replaced by computable equivalents; perhaps at the expense of sacrificing properties of the variational setting.

First-order systems that allow the construction of a L_2 least-squares functional that is H^1-norm equivalent are commonly referred to as H^1-coercive formulations. Such systems yield optimal error estimates with respect to the H^1-norm for all variables and ensure the optimality of multiplicative and additive multigrid methods [9], which could be used either as a solver or a preconditioner for the conjugate gradient method.

The most popular transformation to an equivalent first-order system for the incompressible Navier–Stokes equations is the vorticity based first-order system. In two dimensions the total number of variables is only increased by one and this formulation has the benefit of directly solving for a quantity of physical relevance, the vorticity. However, the velocity–pressure–vorticity first-order system is not H^1-coercive for particular sets of boundary conditions (details are given in [7,10]) and therefore fails to completely emulate a variational setting. Nevertheless, the formulation has had widespread acceptance, and in actual implementations performs exceptionally well [11,12]. Yet another approach is to introduce the stresses as independent variables. This leads to a stress based first-order system. In two dimensions the total number of variables is increased by three; however, the velocity–pressure–stress first-order system is not H^1-coercive, regardless of the choice of boundary conditions [7]. A third option is to introduce all components of the gradient of the velocity vector field as independent variables. By adding additional constraints to weaken the dependencies between variables this equivalent first-order system, hereafter referred to as the velocity gradient based first-order system, is always H^1-coercive [9,13]. In two dimensions the total number of variables is increased by four and this formulation has the added benefit to easily compute (in the post-processing stage) physical quantities of interest that are linear combinations of the partial derivatives of the velocity vector field, e.g., vorticity and stresses.

In the context of least-squares finite element formulations for the Navier–Stokes equations, predominantly low order nodal expansions have been used to develop the discrete finite element model. When the formulation is not H^1-norm equivalent (sometimes referred to as a *quasi-norm-equivalent* or a *non-equivalent* formulation), low order nodal expansions tend to lock and reduced integration techniques must be used to obtain acceptable numerical results. When enough redundant degrees of freedom are constrained the least-squares finite element solution using reduced integration yields a collocation finite element solution. However, the collocation solution may not always be reliable and the least-squares functional cannot be used to measure the quality of the solution.

Even though a *quasi-norm-equivalent* or a *non-equivalent* formulation departs from the ideal mathematical setting, it does not lead to disastrous results; as a violation of the inf–sup condition would, in a mixed weak form Galerkin formulation. Motivation for this study arose from the resiliency of the least-squares method to such departures from the mathematically ideal setting. Furthermore, we refrain from using reduced integration techniques and it is through our work that we wish to advance the practice of full integration and residual minimization through proper *hp*-refinement.

Jiang and Sonnad [14] implemented a *p*-version least-squares formulation for the numerical solution of the stationary incompressible Navier–Stokes equations based on the velocity–pressure–vorticity first-order system. However, no detailed numerical results were reported. Surana and co-workers [15,16] presented numerical results for the stationary incompressible Navier–Stokes stress based first-order system using a *p*-version least-squares formulation based on a modal basis derived from equispaced Lagrange polynomials. Here we consider the numerical solution of the stationary incompressible and low-speed compressible

Navier–Stokes equations using either a vorticity/heat flux or velocity gradient/heat flux based first-order system. We make use of the nodal and modal expansions for quadrilateral elements described by Warburton et al. [17].

The paper is organized as follows. In Section 2, we present the least-squares formulation for the Poisson equation and, via numerical examples, demonstrate spectral convergence of the L_2 least-squares functional and L_2 error norms. We give details on the finite element model and the nodal/modal expansions used throughout the paper. In Section 3, we present the least-squares formulation for the stationary incompressible Navier–Stokes equations. We focus attention on the vorticity and the velocity gradient based first-order systems and verify spectral convergence using the Kovasznay flow solution. We present results for the two-dimensional flow over a backward-facing step, discuss the modeling of outflow boundary conditions, and compare results with the benchmark solution of Gartling [18]. Next, we consider flow past a circular cylinder at low Reynolds number and compare the predicted surface pressure distribution with experimental measurements of Grove et al. [19]. To demonstrate the capabilities of the algorithm for large-scale problems, we present results for the three-dimensional lid-driven cavity flow and compare results with published data of Jiang et al. [20]. In Section 4, we consider the stationary low-speed compressible Navier–Stokes equations. We present results for compressible buoyant flow inside a square enclosure and compare results with the benchmark solution of Yu et al. [21].

2. The Poisson equation

Let $\bar{\Omega}$ be the closure of an open bounded region Ω in $\mathbb{R}^n$, where $n = 2$ or 3 represents the number of space dimensions, and $\mathbf{x} = (x_1, \ldots, x_n) = (x, y, z)$ be a point in $\bar{\Omega} = \Omega \cup \partial\Omega$, where $\partial\Omega = \Gamma$ is the boundary of Ω. We consider the solution of the Poisson equation, which can be stated as follows.

Find $\phi(\mathbf{x})$ such that

$$-\nabla^2\phi = f \quad \text{in } \Omega, \tag{1}$$

$$\phi = \phi^s \quad \text{on } \Gamma_\phi, \tag{2}$$

$$\hat{\mathbf{n}} \cdot \nabla\phi = q_n^s \quad \text{on } \Gamma_q, \tag{3}$$

where $\Gamma = \Gamma_\phi \cup \Gamma_q$ and $\Gamma_\phi \cap \Gamma_q = \emptyset$, f is the source term, $\hat{\mathbf{n}}$ is the outward unit normal on the boundary of Ω, ϕ^s is the prescribed value of ϕ on the boundary Γ_ϕ, and q_n^s is the prescribed normal flux on the boundary Γ_q.

Although direct application of the least-squares variational principle to the Poisson equation is possible, it will result in an impractical least-squares finite element model as we would be required to work with continuously differentiable finite element spaces. Moreover, the resulting condition number of the corresponding discrete problem would be much higher compared with the condition number resulting from application of the weak form Galerkin method to the same problem. We proceed instead by first replacing the Poisson problem, Eqs. (1)–(3), with its first-order system equivalent.

Find $\phi(\mathbf{x})$ and $\mathbf{u}(\mathbf{x})$ such that

$$-\nabla \cdot \mathbf{u} = f \quad \text{in } \Omega, \tag{4}$$

$$\nabla\phi - \mathbf{u} = \mathbf{0} \quad \text{in } \Omega, \tag{5}$$

$$\nabla \times \mathbf{u} = \mathbf{0} \quad \text{in } \Omega, \tag{6}$$

$$\phi = \phi^s \quad \text{on } \Gamma_\phi, \tag{7}$$

$$\hat{\mathbf{n}} \cdot \mathbf{u} = q_n^s \quad \text{on } \Gamma_q, \tag{8}$$

where $\mathbf{u}$ is a vector valued function whose components are the fluxes of ϕ, defined in Eq. (5). For $n = 2$ (the two-dimensional case) we may also specify $\hat{\mathbf{t}} \cdot \mathbf{u} = \hat{\mathbf{t}} \cdot \nabla \phi^s(\mathbf{x})$ on Γ_ϕ, where $\hat{\mathbf{t}}$ is the unit tangent on the boundary of Ω. Similarly for $n = 3$, we may specify $\hat{\mathbf{t}}_1 \cdot \nabla \phi^s(\mathbf{x})$ and $\hat{\mathbf{t}}_2 \cdot \nabla \phi^s(\mathbf{x})$ on Γ_ϕ, where $\hat{\mathbf{t}}_1$ and $\hat{\mathbf{t}}_2$ are unit tangent vectors on the boundary of Ω. Eq. (6) is a curl constraint to ensure H^1-coercivity of the system [7].

2.1. L_2 least-squares formulation

For $s \geqslant 0$, we use the standard notation and definition for the Sobolev spaces $H^s(\Omega)$ and $H^s(\Gamma)$ with corresponding inner products denoted by $(\cdot,\cdot)_{s,\Omega}$ and $(\cdot,\cdot)_{s,\Gamma}$ and norms by $\|\cdot\|_{s,\Omega}$ and $\|\cdot\|_{s,\Gamma}$, respectively. Whenever there is no chance of ambiguity, the measures Ω and Γ will be omitted from inner product and norm designations. We denote the $L_2(\Omega)$ and $L_2(\Gamma)$ inner products by $(\cdot,\cdot)$ and $(\cdot,\cdot)_\Gamma$, respectively. By $\mathbf{H}^s(\Omega)$ we denote the product space $[H^s(\Omega)]^n$. We denote by $H_0^1(\Omega)$ the space consisting of $H^1(\Omega)$ functions that vanish on the boundary Γ and by $\bar{L}_2(\Omega)$ the space of all square integrable functions with zero mean with respect to Ω.

The L_2 least-squares functional associated with the equivalent first-order system of the Poisson problem is

$$\mathscr{J}(\phi, \mathbf{u}; f) = \frac{1}{2}\left(\| - \nabla \cdot \mathbf{u} - f \|_0^2 + \| \nabla \phi - \mathbf{u} \|_0^2 + \| \nabla \times \mathbf{u} \|_0^2 \right). \tag{9}$$

Considering homogeneous boundary data, the least-squares principle for functional (9) can be stated as

Find $(\phi, \mathbf{u}) \in \mathbf{X}$ such that for all $(\psi, \mathbf{v}) \in \mathbf{X}$

$$\mathscr{J}(\phi, \mathbf{u}; f) \leqslant \mathscr{J}(\psi, \mathbf{v}; f), \tag{10}$$

where we use the space

$$\mathbf{X} = \left\{ (\phi, \mathbf{u}) \in H^1(\Omega) \times \mathbf{H}^1(\Omega) \,\middle|\, \phi|_{\Gamma_\phi} = 0,\ \hat{\mathbf{n}} \cdot \mathbf{u}|_{\Gamma_q} = 0 \right\}.$$

It is easy to see that the Euler–Lagrange equation for this minimization problem is given by the following variational problem [2]:

Find $(\phi, \mathbf{u}) \in \mathbf{X}$ such that for all $(\psi, \mathbf{v}) \in \mathbf{X}$

$$\mathscr{B}((\phi, \mathbf{u}), (\psi, \mathbf{v})) = \mathscr{F}((\psi, \mathbf{v})), \tag{11}$$

where

$$\mathscr{B}((\phi, \mathbf{u}), (\psi, \mathbf{v})) = \int_\Omega (-\nabla \cdot \mathbf{u})\ (-\nabla \cdot \mathbf{v})\, \mathrm{d}\Omega + \int_\Omega (\nabla \phi - \mathbf{u}) \cdot (\nabla \psi - \mathbf{v})\, \mathrm{d}\Omega + \int_\Omega (\nabla \times \mathbf{u}) \cdot (\nabla \times \mathbf{v})\, \mathrm{d}\Omega$$

and

$$\mathscr{F}((\psi,\mathbf{v})) = \int_{\Omega} f(-\nabla\cdot\mathbf{v})\,\mathrm{d}\Omega.$$

2.2. Finite element model

The finite element model is obtained by either restricting (11) to the finite dimensional subspace $\mathbf{X}_{hp}$ of the infinite dimensional space $\mathbf{X}$, or equivalently by minimizing (9) with respect to the chosen approximating spaces. Then the least-squares discrete finite element model for the Poisson equation is given by the following discrete variational problem:

Find $(\phi^{hp},\mathbf{u}^{hp})\in\mathbf{X}_{hp}$ such that for all $(\psi^{hp},\mathbf{v}^{hp})\in\mathbf{X}_{hp}$

$$\mathscr{B}((\phi^{hp},\mathbf{u}^{hp}),(\psi^{hp},\mathbf{v}^{hp})) = \mathscr{F}((\psi^{hp},\mathbf{v}^{hp})). \tag{12}$$

We proceed to define a discrete problem by choosing appropriate finite element subspaces for ϕ and each of the components of the vector valued function $\mathbf{u}=(u,v,w)$. There are no restrictive compatibility conditions on the discrete spaces, so we choose the same finite element subspace for each of the primary variables. The only requirement on the approximating spaces is that we choose continuous piecewise polynomials that are at least bi-linear (in two dimensions) or tri-linear (in three dimensions).

Consider the two-dimensional case and let $\mathscr{P}_{\mathrm{h}}=\{\mathscr{Q}\}$ be a family of quadrilateral finite elements $\bar{\Omega}_e$ that make up the connected model $\bar{\Omega}^h$. We map $\bar{\Omega}_e$ to a bi-unit square $\hat{\Omega}_e=[-1,1]\times[-1,1]$, where $\boldsymbol{\xi}=(\xi_1,\xi_2)=(\xi,\eta)$ is a point in $\hat{\Omega}_e$. Over a typical element $\hat{\Omega}_e$, we approximate ϕ by the expression

$$\phi(\xi,\eta)\approx\phi^{hp}(\xi,\eta)=\sum_{j=1}^{n}\Delta_j\varphi_j(\xi,\eta)\quad\text{in }\hat{\Omega}_e. \tag{13}$$

In a modal expansion, φ_j are tensor products of the one-dimensional C^0 p-type hierarchical basis

$$\psi_i(\xi)=\begin{cases}\frac{1-\xi}{2}, & i=1,\\ \left(\frac{1-\xi}{2}\right)\left(\frac{1+\xi}{2}\right)P_{p-2}^{\alpha,\beta}, & 2\leqslant i\leqslant p,\ p\geqslant 2,\\ \frac{1+\xi}{2}, & i=p+1\end{cases} \tag{14}$$

and Δ_j are coefficients associated with each of the modes of the hierarchical basis. In definition (14), $P_p^{\alpha,\beta}$ are the Jacobi polynomials of order p. We use ultraspheric polynomials corresponding to the choice $\alpha=\beta$ with $\alpha=\beta=0$ or 1.

In a nodal expansion, φ_j are tensor products of the one-dimensional C^0 spectral nodal basis

$$h_i(\xi)=\frac{(\xi-1)(\xi+1)L_p'(\xi)}{p(p+1)L_p(\xi_i)(\xi-\xi_i)} \tag{15}$$

and Δ_j are nodal values due to the Kronecker delta property of the spectral basis. In Eq. (15), $L_p=P_p^{0,0}$ is the Legendre polynomial of order p and ξ_i denotes the location of the roots of $(\xi-1)(\xi+1)L_p'(\xi)=0$ in the interval $[-1,1]$. Details on the multidimensional construction of both the modal and nodal expansions can be found in [1].

We approximate the components of the vector valued function $\mathbf{u}=(u,v)$ in similar manner as we did for ϕ in Eq. (13) and proceed to generate a system of linear algebraic equations at the element level using Eq. (12). The integrals in Eq. (12) are evaluated using Gauss quadrature rules. In our implementation the Gauss–Legendre rules are used for both the modal and nodal expansions, and *full integration* is used to evaluate the integrals.

The global system of equations is assembled from the element contributions using the direct stiffness summation approach. The assembled system of equations can be written as

$$\begin{pmatrix} [K^{11}] & [K^{12}] & [K^{13}] \\ [K^{12}]^{\mathrm{T}} & [K^{22}] & [K^{23}] \\ [K^{13}]^{\mathrm{T}} & [K^{23}]^{\mathrm{T}} & [K^{33}] \end{pmatrix} \begin{pmatrix} \{\Delta^1\} \\ \{\Delta^2\} \\ \{\Delta^3\} \end{pmatrix} = \begin{pmatrix} \{F^1\} \\ \{F^2\} \\ \{F^3\} \end{pmatrix},$$

where $\{\Delta^1\}$, $\{\Delta^2\}$, $\{\Delta^3\}$ are the modal/nodal unknown coefficients associated with ϕ, u, and v. For details on standard finite element methods, such as mapping $\bar{\Omega}_e \rightleftarrows \hat{\Omega}_e$, numerical integration in $\hat{\Omega}_e$, and assembly using the direct stiffness summation approach, see [22,23].

2.3. Numerical example

Consider the case where $\bar{\Omega} = [-1,1] \times [-1,1]$. Fig. 1 shows the connected model $\bar{\Omega}^h$, where the set $\{\mathcal{Q}\}$ consists of four quadrilateral finite elements $\bar{\Omega}_e$.

We seek a function $\phi(x,y)$ satisfying the Poisson problem subject to the boundary conditions (see Fig. 1)

$$\frac{\partial \phi}{\partial y} = v = 0 \quad \text{on } \Gamma_a,$$
$$\phi = \phi^s(y) \quad \text{on } \Gamma_b,$$
$$\frac{\partial \phi}{\partial y} = v = 0 \quad \text{on } \Gamma_c,$$
$$\frac{\partial \phi}{\partial x} = u = q^s(y) \quad \text{on } \Gamma_d.$$

The functions $f(x,y)$, $\phi^s(y)$, and $q^s(y)$ are chosen such that the analytical solution $\phi(x,y)$ is

$$\phi(x,y) = (7x + x^7)\cos(\pi y).$$

We use the modal expansions for quadrilateral elements based on the ultraspheric Jacobi polynomials with weights equal to zero, i.e., the Legendre polynomials. The resulting linear system of equations with a SPD coefficient matrix is solved using Cholesky factorization. In Fig. 2, we plot the L_2 least-squares functional

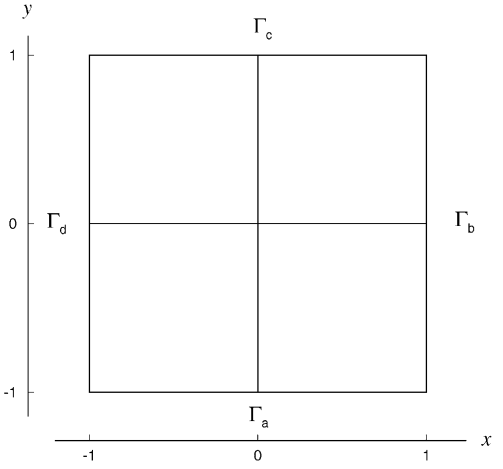

Fig. 1. A uniform mesh of four elements is shown on the bi-unit square on which the Poisson problem is defined.

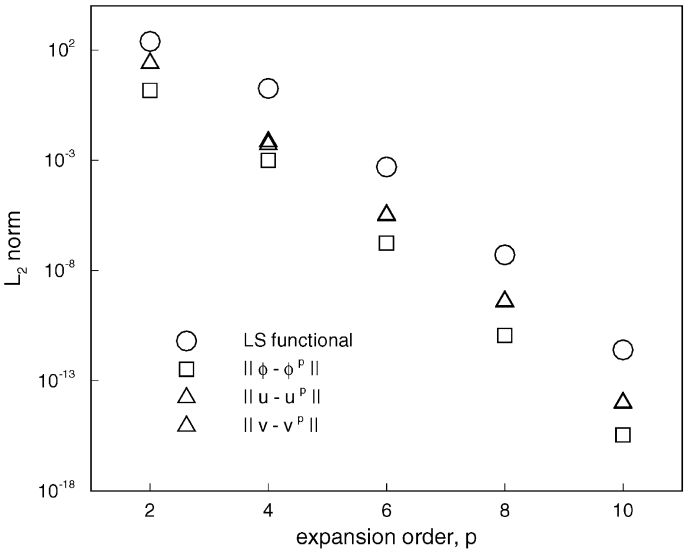

Fig. 2. Decay of the least-squares functional and convergence of the primary variables to the exact solution of the Poisson problem in the L_2-norm.

($\mathscr{J}$) and the L_2 error of the three primary variables (ϕ, u, v) as a function of the expansion order in a logarithmic-linear scale. Exponentially fast decay (spectral convergence) of the L_2 least-squares functional and L_2 errors is observed, i.e., doubling the degrees of freedom per direction results in *more* than two orders of magnitude reduction in discretization errors.

3. The incompressible Navier–Stokes equations

We consider the solution of the stationary Navier–Stokes equations governing incompressible flow, which in dimensionless form can be stated as follows:

Find the velocity $\mathbf{u}(\mathbf{x})$ and pressure $p(\mathbf{x})$ such that

$$(\mathbf{u}\cdot\nabla)\mathbf{u}+\nabla p-\frac{1}{Re}\nabla\cdot\left[(\nabla\mathbf{u})+(\nabla\mathbf{u})^{\mathrm{T}}\right]=\mathbf{f}\quad\text{in }\Omega, \tag{16}$$

$$\nabla\cdot\mathbf{u}=0\quad\text{in }\Omega, \tag{17}$$

$$\mathbf{u}=\mathbf{u}^{s},\quad\text{on }\Gamma_u, \tag{18}$$

$$\hat{\mathbf{n}}\cdot\boldsymbol{\sigma}=\mathbf{f}^{s}\quad\text{on }\Gamma_f, \tag{19}$$

where $\Gamma=\Gamma_u\cup\Gamma_f$ and $\Gamma_u\cap\Gamma_f=\emptyset$, Re is the Reynolds number, $\boldsymbol{\sigma}=-p\mathbf{I}+1/Re\,[(\nabla\mathbf{u})+(\nabla\mathbf{u})^{\mathrm{T}}]$, $\mathbf{f}$ is a dimensionless force, $\hat{\mathbf{n}}$ is the outward unit normal on the boundary of Ω, $\mathbf{u}^{s}$ is the prescribed velocity on the boundary Γ_u, and $\mathbf{f}^{s}$ are the prescribed tractions on the boundary Γ_f. We assume that the problem is well posed and that a unique solution exists.

In situations where outflow boundary conditions need to be modeled, the Navier–Stokes equations in the $\nabla^2\mathbf{u}$ form are preferred [24]. In such cases, (using the incompressibility constraint given in Eq. (17)) we would drop the $(\nabla\mathbf{u})^{\mathrm{T}}$ term in Eq. (16), and the boundary conditions in Eq. (19) would then become

$$\hat{\mathbf{n}} \cdot \tilde{\boldsymbol{\sigma}} = \tilde{\mathbf{f}}^s \quad \text{on } \Gamma_f, \tag{20}$$

where $\tilde{\boldsymbol{\sigma}}$ is a pseudo-stress, $\tilde{\boldsymbol{\sigma}} = -p\mathbf{I} + (1/Re)\nabla\mathbf{u}$, and $\tilde{\mathbf{f}}^s$ are the prescribed pseudo-tractions on the boundary Γ_f.

3.1. The vorticity based first-order system

Introducing the vorticity vector, $\boldsymbol{\omega} = \nabla \times \mathbf{u}$, then by making use of the vector identity

$$\nabla \times \nabla \times \mathbf{u} = -\nabla^2\mathbf{u} + \nabla(\nabla \cdot \mathbf{u})$$

and in view of the incompressibility constraint given in Eq. (17), the stationary Navier–Stokes equations, Eqs. (16)–(19), can be replaced by their first-order system equivalent:

Find the velocity $\mathbf{u}(\mathbf{x})$, pressure $p(\mathbf{x})$, and vorticity $\boldsymbol{\omega}(\mathbf{x})$ such that

$$(\mathbf{u} \cdot \nabla)\mathbf{u} + \nabla p + \frac{1}{Re}\nabla \times \boldsymbol{\omega} = \mathbf{f} \quad \text{in } \Omega, \tag{21}$$

$$\boldsymbol{\omega} - \nabla \times \mathbf{u} = \mathbf{0} \quad \text{in } \Omega, \tag{22}$$

$$\nabla \cdot \mathbf{u} = 0 \quad \text{in } \Omega, \tag{23}$$

$$\nabla \cdot \boldsymbol{\omega} = 0 \quad \text{in } \Omega, \tag{24}$$

$$\mathbf{u} = \mathbf{u}^s \quad \text{on } \Gamma_u, \tag{25}$$

$$\boldsymbol{\omega} = \boldsymbol{\omega}^s \quad \text{on } \Gamma_\omega. \tag{26}$$

The seemingly redundant equation (24) is needed in the three-dimensional case to make the system of equations uniformly elliptic [7]. Typically $\Gamma_u \cap \Gamma_\omega = \emptyset$, i.e., if velocity is specified at a boundary, vorticity need not be specified there. Outflow boundary conditions are treated through the least-squares functional and will be discussed in Section 3.3.2.

3.1.1. L_2 least-squares formulation

The L_2 least-squares functional associated with the velocity–pressure–vorticity formulation is given by

$$\mathscr{J}(\mathbf{u}, p, \boldsymbol{\omega}; \mathbf{f}) = \frac{1}{2}\left(\left\|(\mathbf{u} \cdot \nabla)\mathbf{u} + \nabla p + \frac{1}{Re}\nabla \times \boldsymbol{\omega} - \mathbf{f}\right\|_0^2 + \|\boldsymbol{\omega} - \nabla \times \mathbf{u}\|_0^2 + \|\nabla \cdot \mathbf{u}\|_0^2 + \nabla \cdot \boldsymbol{\omega}\|_0^2\right). \tag{27}$$

This L_2 functional does not define an equivalent norm in $H^1(\Omega)$ when augmented by a pure velocity boundary condition ($\Gamma = \Gamma_u$). As we show later by numerical examples, in practice, the formulation performs exceptionally well and seems to be unaffected by this departure from the ideal mathematical setting. Considering the homogeneous pure velocity boundary condition case, the least-squares principle for functional (27) can be stated as

Find $(\mathbf{u}, p, \boldsymbol{\omega}) \in \mathbf{X}$ such that for all $(\mathbf{v}, q, \boldsymbol{\psi}) \in \mathbf{X}$

$$\mathscr{J}(\mathbf{u}, p, \boldsymbol{\omega}; \mathbf{f}) \leqslant \mathscr{J}(\mathbf{v}, q, \boldsymbol{\psi}; \mathbf{f}), \tag{28}$$

where we use the space

$$\mathbf{X} = \left\{ (\mathbf{u}, p, \boldsymbol{\omega}) \in \mathbf{H}_0^1(\Omega) \times H^1(\Omega) \cap \bar{L}_2(\Omega) \times \mathbf{H}^1(\Omega) \right\}.$$

The Euler–Lagrange equation for this minimization problem is given by the following variational problem:

Find $(\mathbf{u}, p, \boldsymbol{\omega}) \in \mathbf{X}$ such that for all $(\mathbf{v}, q, \boldsymbol{\psi}) \in \mathbf{X}$

$$\mathscr{B}((\mathbf{u}, p, \boldsymbol{\omega}), (\mathbf{v}, q, \boldsymbol{\psi})) = \mathscr{F}((\mathbf{v}, q, \boldsymbol{\psi})), \tag{29}$$

where

$$\mathscr{B}((\mathbf{u}, p, \boldsymbol{\omega}), (\mathbf{v}, q, \boldsymbol{\psi})) = \int_\Omega \left((\mathbf{u} \cdot \nabla)\mathbf{u} + \nabla p + \frac{1}{Re} \nabla \times \boldsymbol{\omega} \right) \cdot \left((\mathbf{v} \cdot \nabla)\mathbf{v} + \nabla q + \frac{1}{Re} \nabla \times \boldsymbol{\psi} \right) \mathrm{d}\Omega + \int_\Omega (\boldsymbol{\omega} - \nabla \times \mathbf{u}) \cdot (\boldsymbol{\psi} - \nabla \times \mathbf{v}) \, \mathrm{d}\Omega + \int_\Omega (\nabla \cdot \mathbf{u}) \, (\nabla \cdot \mathbf{v}) \, \mathrm{d}\Omega + \int_\Omega (\nabla \cdot \boldsymbol{\omega}) \, (\nabla \cdot \boldsymbol{\psi}) \, \mathrm{d}\Omega$$

and

$$\mathscr{F}((\mathbf{v}, q, \boldsymbol{\psi})) = \int_\Omega \mathbf{f} \cdot \left((\mathbf{v} \cdot \nabla)\mathbf{v} + \nabla q + \frac{1}{Re} \nabla \times \boldsymbol{\psi} \right) \mathrm{d}\Omega.$$

3.1.2. Finite element model

The finite element model is obtained by either restricting (29) to the finite dimensional subspace $\mathbf{X}_{hp}$ of the infinite dimensional space $\mathbf{X}$, or equivalently by minimizing (27) with respect to the chosen approximating spaces. Then the least-squares discrete finite element model for the incompressible Navier–Stokes equations is given by the following discrete variational problem:

Find $(\mathbf{u}^{hp}, p^{hp}, \boldsymbol{\omega}^{hp}) \in \mathbf{X}_{hp}$ such that for all $(\mathbf{v}^{hp}, q^{hp}, \boldsymbol{\psi}^{hp}) \in \mathbf{X}_{hp}$

$$\mathscr{B}\left((\mathbf{u}^{hp}, p^{hp}, \boldsymbol{\omega}^{hp}), (\mathbf{v}^{hp}, q^{hp}, \boldsymbol{\psi}^{hp}) \right) = \mathscr{F}\left((\mathbf{v}^{hp}, q^{hp}, \boldsymbol{\psi}^{hp}) \right). \tag{30}$$

We proceed to define a discrete problem by choosing appropriate finite element subspaces for the velocity, pressure, and vorticity. There are no restrictive compatibility conditions on the discrete spaces, so we choose the same finite element subspace for all primary variables. Following the procedure outlined for the Poisson problem, we generate a system of equations for the modal/nodal unknown coefficients associated with velocity, pressure, and vorticity. Once the discrete problem is obtained, it is then linearized by Newton's method.

3.2. The velocity gradient based first-order system

To define the first-order velocity–pressure–velocity gradient system, we introduce all components of the gradient of the velocity vector field as independent variables. Viewing the n-vector functions as column vectors and the new n^2-vector functions as either block column vectors or matrices, using the notation of [9], we define the velocity gradients, $\underline{\mathbf{U}}$, as follows:

$$\underline{\mathbf{U}} = \nabla(\mathbf{u})^{\mathrm{T}}.$$

In terms of $\underline{\mathbf{U}}$, the stationary Navier–Stokes equations, Eqs. (16)–(19), can be replaced by their first-order system equivalent:

Find the velocity $\mathbf{u}(\mathbf{x})$, pressure $p(\mathbf{x})$, and velocity gradients $\underline{\mathbf{U}}(\mathbf{x})$ such that

$$(\mathbf{u} \cdot \underline{\mathbf{U}})^{\mathrm{T}} + \nabla p - \frac{1}{Re} (\nabla \cdot \underline{\mathbf{U}})^{\mathrm{T}} = \mathbf{f} \quad \text{in } \Omega, \tag{31}$$

$$\underline{\mathbf{U}} - \nabla(\mathbf{u})^{\mathrm{T}} = \underline{\mathbf{0}} \quad \text{in } \Omega, \tag{32}$$

$$\nabla \cdot \mathbf{u} = 0 \quad \text{in } \Omega, \tag{33}$$

$$\nabla \times \underline{\mathbf{U}} = \underline{\mathbf{0}} \quad \text{in } \Omega, \tag{34}$$

$$\nabla(\mathrm{tr}\,\underline{\mathbf{U}}) = \mathbf{0} \quad \text{in } \Omega, \tag{35}$$

$$\mathbf{u} = \mathbf{u}^s \quad \text{on } \Gamma_u, \tag{36}$$

$$U_{ij} = U_{ij}^s \quad \text{on } \Gamma_U, \tag{37}$$

where $\mathrm{tr}\,\underline{\mathbf{U}} = \sum_{i=1}^{n} U_{ii}$. For $n = 2$ (the two-dimensional case) we may also specify $\hat{\mathbf{t}} \cdot \underline{\mathbf{U}} = \hat{\mathbf{t}} \cdot \nabla(\mathbf{u}^s(\mathbf{x}))^{\mathrm{T}}$ on Γ_u, where $\hat{\mathbf{t}}$ is the unit tangent on the boundary of Ω. Similarly, for $n = 3$, we may specify $\hat{\mathbf{t}}_1 \cdot \nabla(\mathbf{u}^s(\mathbf{x}))^{\mathrm{T}}$ and $\hat{\mathbf{t}}_2 \cdot \nabla(\mathbf{u}^s(\mathbf{x}))^{\mathrm{T}}$ on Γ_u, where $\hat{\mathbf{t}}_1$ and $\hat{\mathbf{t}}_2$ are unit tangent vectors on the boundary of Ω.

This first-order decomposition is the vector equivalent to that of the Poisson problem. The seemingly redundant equations (34) and (35) are needed to make the system achieve H^1-coercivity [9,13]. The L_2 least-squares formulation and finite element model proceed in a similar manner as that described for the vorticity based first-order system and are not detailed here.

3.3. Numerical examples

In the following, we present numerical results obtained with the proposed formulation. The problems have been selected to assess the predictive capabilities of the vorticity and velocity gradient based finite element models. We start by verifying spectral convergence of the numerical algorithm using and exact solution to the Navier–Stokes equations. Next, we consider the steady two-dimensional flow of incompressible fluid over a backward-facing step and around a circular cylinder. In the last example, we consider the three-dimensional lid-driven cavity problem.

3.3.1. Kovasznay flow

We consider two-dimensional, steady flow in $\bar{\Omega} = [-0.5, 1.5] \times [-0.5, 1.5]$. We use Kovasznay's solution [25] to the stationary incompressible Navier–Stokes equations to verify spectral convergence of the numerical algorithm. The solution is given by

$$u = 1 - \mathrm{e}^{\lambda x}\cos(2\pi y), \quad v = \frac{\lambda}{2\pi}\mathrm{e}^{\lambda x}\sin(2\pi y), \quad p = p_0 - \frac{1}{2}\mathrm{e}^{2\lambda x},$$

where $\lambda = Re/2 - (Re^2/4 + 4\pi^2)^{1/2}$ and p_0 is a reference pressure (an arbitrary constant). Fig. 3(a) shows u-velocity contours of the exact solution for $Re = 40$. Fig. 3(b) shows the discretization of the domain using a non-uniform mesh of eight quadrilateral finite elements $\bar{\Omega}_e$.

The incompressible Navier–Stokes equations in the vorticity based first-order form is used to develop the finite element model. *Nodal* expansions (spectral elements) are used to obtain the discrete model. The exact solution is used to prescribe Dirichlet velocity boundary conditions on Γ and pressure is specified at a point. No boundary conditions for the vorticity are necessary. The discrete system was linearized using Newton's method and the resulting linear algebraic system of equations with a SPD coefficient matrix solved using Cholesky factorization at each Newton step. Nonlinear convergence was declared when the relative norm of the residual in velocities, $\|\Delta\mathbf{u}^{hp}\|/\|\mathbf{u}^{hp}\|$, was less than 10^{-4}, which typically required five Newton iterations. In Fig. 4 we plot the L_2 least-squares functional and L_2 error of the velocity, pressure, and vorticity fields as

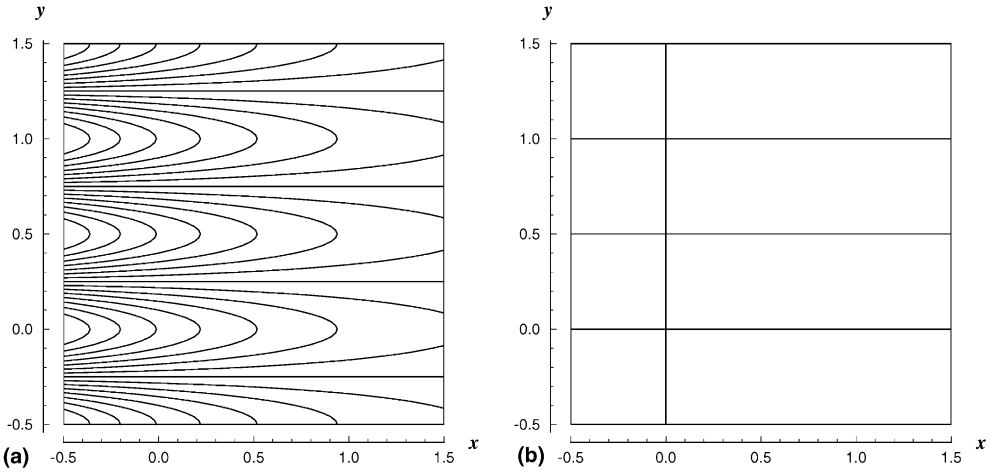

Fig. 3. Kovasznay flow: (a) u-velocity contours of the exact solution for $Re = 40$; (b) computational domain using eight quadrilateral elements.

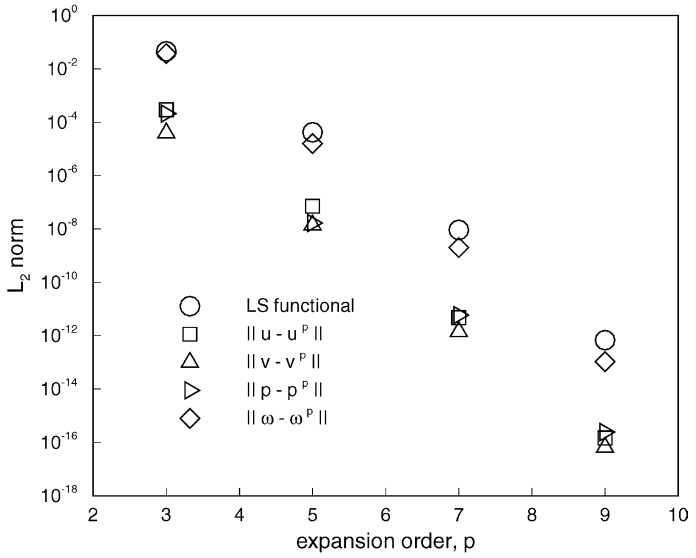

Fig. 4. Decay of the least-squares functional and convergence of the velocity, pressure, and vorticity fields to the exact Kovasznay solution in the L_2-norm. Nodal expansion.

a function of the expansion order in a logarithmic-linear scale. Even though functional (27) defines a *non-equivalent* formulation for the pure velocity boundary condition, spectral convergence of the L_2 least-squares functional and L_2 error is observed. Spectral convergence was also verified when *modal* expansions were used to obtain the discrete model.

We perform the same analysis for the incompressible Navier–Stokes equations in the velocity gradient based first-order form using *modal* expansions. This system leads to a L_2 least-squares functional that defines an equivalent norm in $H^1(\Omega)$. In Fig. 5 we plot the L_2 least-squares functional and L_2 error of the velocity, pressure, and velocity gradient fields as a function of the expansion order in a logarithmic-linear

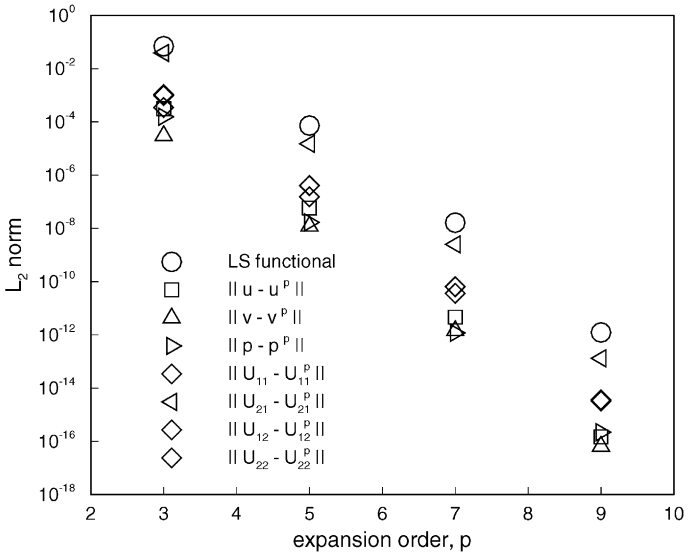

Fig. 5. Decay of the least-squares functional and convergence of the velocity, pressure, and velocity gradient fields to the exact Kovasznay solution in the L_2-norm. Modal expansion.

scale. Spectral convergence of the L_2 least-squares functional and L_2 error is observed. Spectral convergence was also verified when *nodal* expansions were used to obtain the discrete model.

Both the *non-equivalent* and *norm-equivalent* formulations achieve spectral convergence. Clearly, the fact that functional (27) is not H^1-norm equivalent and hence defines a *non-equivalent* formulation for the pure velocity boundary condition case; does not imply that the method is not optimal. It simply means that the optimality of the resulting method cannot be established a priori using standard elliptic theory. Similar observations were reported by Proot and Gerrtisma [26], for *non-equivalent* and *norm-equivalent* formulations, when verifying spectral convergence for the vorticity based first-order Stokes equations.

Considering the convergence rate and accuracy of the numerical solution, both the vorticity and velocity gradient based first-order systems yield similar results. In terms of computer memory requirements and CPU solve time (using Cholesky factorization), the vorticity based first-order system is preferred because it has fewer degrees of freedom. For $n = 2$ (the two-dimensional case) the vorticity first-order decomposition introduces only one component of the vorticity vector as an additional variable, whereas the velocity gradient first-order decomposition introduces four additional variables: $\partial u_i/\partial x_j$, $i, j = 1, 2$. For $n = 3$ the vorticity first-order decomposition introduces the three components of the vorticity vector as additional variables, whereas the velocity gradient first-order decomposition introduces nine additional variables: $\partial u_i/\partial x_j$, $i, j = 1, 2, 3$. A cost comparison between the vorticity and velocity gradient based formulation for the Kovasznay problem is illustrated in Fig. 6, by plotting the L_2 error of the velocity field as a function of the total number of degrees of freedom in a logarithmic-linear scale. Clearly, the vorticity based formulation is preferred because, for a given number of degrees of freedom, it allows for a more accurate solution at higher p-levels.

3.3.2. Flow over a backward-facing step

We consider two-dimensional, steady flow over a backward-facing step at $Re = 800$. The geometry and boundary conditions are taken from the benchmark solution of Gartling [18] and are shown in Fig. 7. As shown in Fig. 7 the standard step geometry was simplified by excluding the channel portion upstream of the step. The boundary conditions for the step geometry include the no-slip condition at all solid surfaces and a

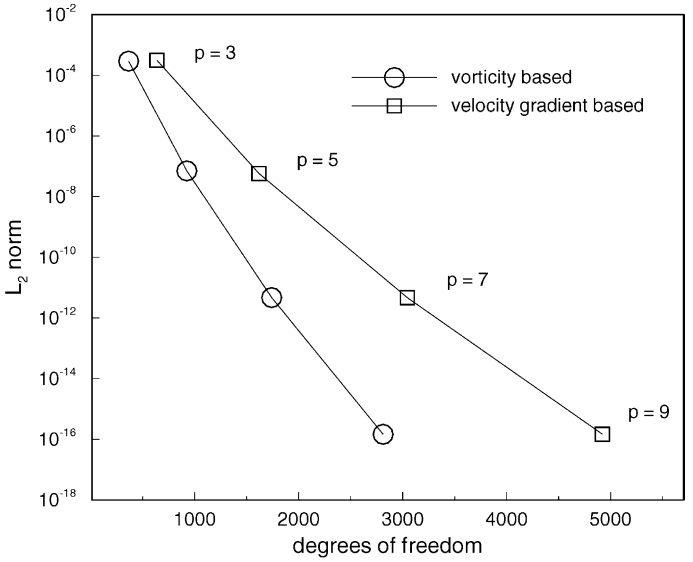

Fig. 6. Convergence of the velocity field to the exact Kovasznay solution in the L_2-norm for the vorticity and velocity gradient based first-order systems. Nodal expansion.

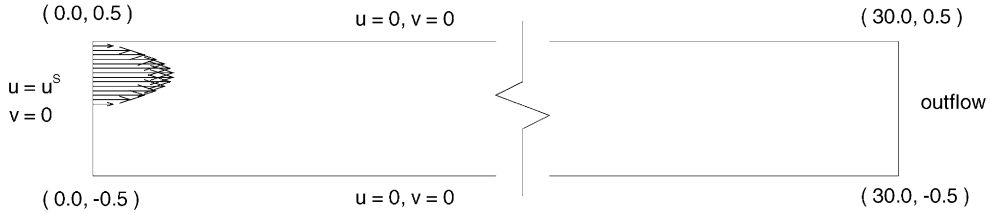

Fig. 7. Geometry and boundary conditions for flow over a backward-facing step.

parabolic inlet velocity profile given by $u(y) = 24y(0.5 - y)$ for $0 \leqslant y \leqslant 0.5$. The Reynolds number is based on the mean inlet velocity.

The outflow boundary condition is of relevance in the context of the least-squares finite element formulation and is discussed in the following. Instead of imposing an outflow boundary condition in a strong sense we impose it in a weak sense through the least-squares functional. For example, if we use the vorticity based first-order system the L_2 least-squares functional is now

$$\mathscr{J}(\mathbf{u}, p, \boldsymbol{\omega}; \mathbf{f}) = \frac{1}{2}\left(\left\| (\mathbf{u}\cdot\nabla)\mathbf{u} + \nabla p + \frac{1}{Re}\nabla\times\boldsymbol{\omega} - \mathbf{f} \right\|_0^2 + \|\boldsymbol{\omega} - \nabla\times\mathbf{u}\|_0^2 + \|\nabla\cdot\mathbf{u}\|_0^2 + \|\nabla\cdot\boldsymbol{\omega}\|_0^2 + \|\hat{\mathbf{n}}\cdot\tilde{\boldsymbol{\sigma}} - \tilde{\mathbf{f}}^s\|_{0,\Gamma_{\text{outflow}}}^2 \right), \tag{38}$$

where $\tilde{\boldsymbol{\sigma}}$ is a pseudo-stress (see Eq. (20)), $\tilde{\boldsymbol{\sigma}} = -p\mathbf{I} + (1/Re)\nabla\mathbf{u}$, and $\tilde{\mathbf{f}}^s$ are the prescribed pseudo-tractions, typically taken to be zero at an outflow boundary. The strong outflow boundary condition $p = 0$ for the vorticity based first-order system or $p = 0$, $\partial v/\partial n = 0$ for the velocity gradient based first-order system also

give good results. However, we prefer the weak imposition of outflow boundary conditions through the least-squares functional as it allows for more freedom in their modelling.

We discretize the domain, $\bar{\Omega} = [0, 30] \times [-0.5, 0.5]$, using 20 finite elements: two elements along the height of the channel and 10 uniformly spaced elements along the length of the channel. The numerical simulation is performed using the two-dimensional incompressible Navier–Stokes equations in the vorticity based first-order form. We use a 11th order modal expansion in each element and linearize the resulting discrete model (having a total of 10,212 degrees of freedom) using Newton's method. At each Newton step, the linear system of equations with a SPD coefficient matrix is solved using the conjugate gradient method with a symmetric Gauss–Seidel preconditioner; see [27]. Convergence of the conjugate gradient method was declared when the norm of the residual was less than 10^{-6}. Nonlinear convergence was declared when the relative norm of the residual in velocities, $\|\Delta \mathbf{u}^{hp}\|/\|\mathbf{u}^{hp}\|$, was less than 10^{-4}, which typically required four Newton iterations. The analysis starts with $Re = 100$ and steps to $Re = 800$ using a solution continuation technique with increments of $Re = 100$. Away from the corner of the step at $(x, y) = (0, 0)$, the L_2 least-squares functional remained below 10^{-5} through the Reynolds number stepping.

Fig. 8 shows the streamlines, the vector velocity field, and pressure contours for $0 \leqslant x \leqslant 10$, where most of the interesting flow structures occur. The flow separates at the step corner and forms a large recirculation region with a reattachment point on the lower wall of the channel at approximately $x = 6$. A second recirculation region forms on the upper wall of the channel beginning near $x = 5$ with a reattachment point at approximately $x = 10.5$.

Fig. 9 shows u-velocity profiles along the channel height at $x = 7$ and $x = 15$. We compare with tabulated values from the benchmark solution of Gartling [18] and find excellent agreement. Gartling's benchmark solution is based on a mixed weak form Galerkin formulation using discretizations ranging from 6×120 to 40×800 bi-quadratic elements, corresponding to discrete systems of 8426 to 355,362 degrees of freedom, respectively. Fig. 10 shows pressure profiles along the length of the channel walls. The slopes of the pressure profiles become constant near the exit plane, meaning that the flow has recovered to fully developed conditions at the exit.

In Fig. 11 we present the convergence history of the preconditioned conjugate gradient (PCG) method using a Jacobi preconditioner and a symmetric Gauss–Seidel preconditioner. The algebraic set of equations being solved corresponds to the 11th order modal expansion discrete model (having a total of 10,212

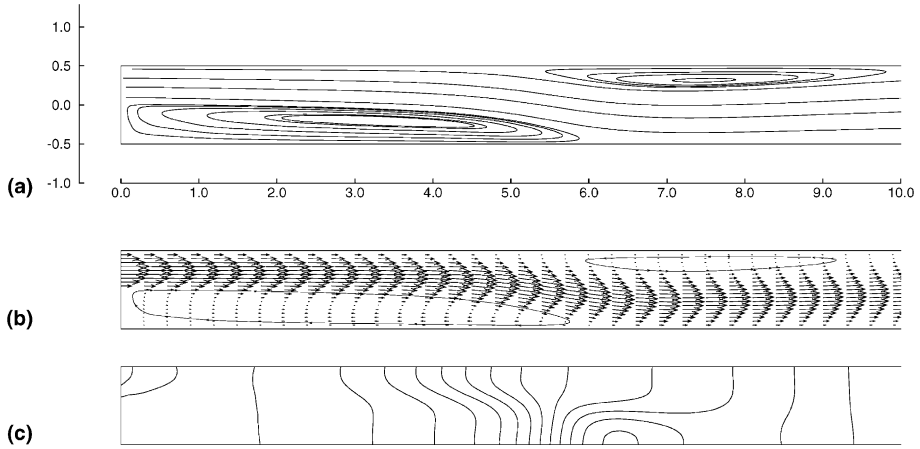

Fig. 8. Flow over a backward-facing step at $Re = 800$: (a) streamlines, (b) vector velocity field, and (c) pressure field. Modal expansion of order 11 using two elements along the height and 10 uniformly spaced elements along the entire length of the channel.

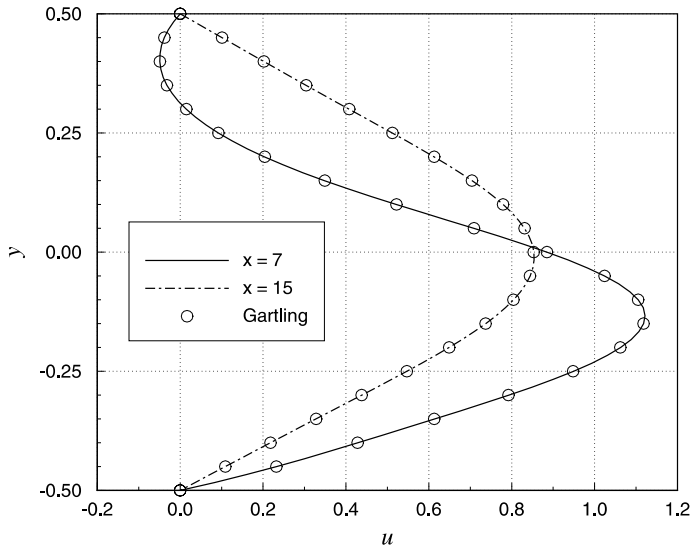

Fig. 9. Flow over a backward-facing step at $Re = 800$: horizontal velocity profiles along the height of the channel at $x = 7$ and $x = 15$. Comparison with the benchmark solution of Gartling [18].

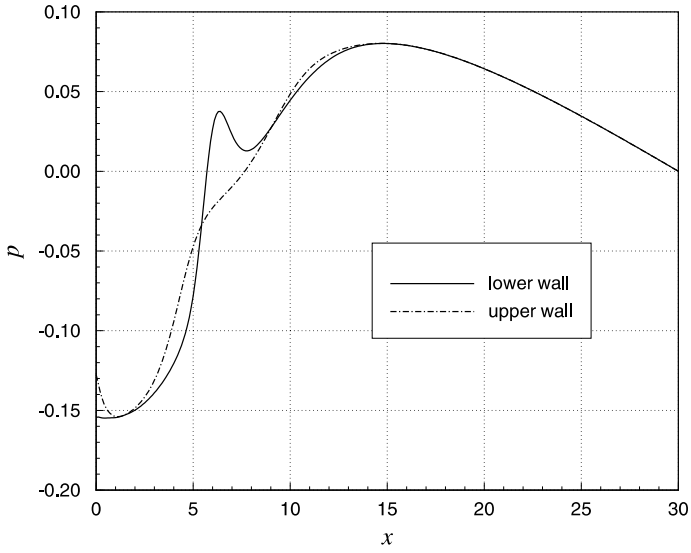

Fig. 10. Flow over a backward-facing step at $Re = 800$: pressure profiles along lower and upper walls of the channel.

degrees of freedom) and flow conditions of $Re = 800$. We plot the convergence history corresponding to each of the four Newton iterations, after which the nonlinear tolerance is achieved. The number of PCG iterations reduces during the nonlinear iteration procedure because a continuation technique is used with respect to the nonlinear loop, i.e., the last converged solution is used as an initial guess for the PCG solver. As expected, the Gauss–Seidel preconditioner gives a higher convergence rate. It should be noted, however, that to apply the Gauss–Seidel preconditioner the assembled system of equations needs to be stored, this is

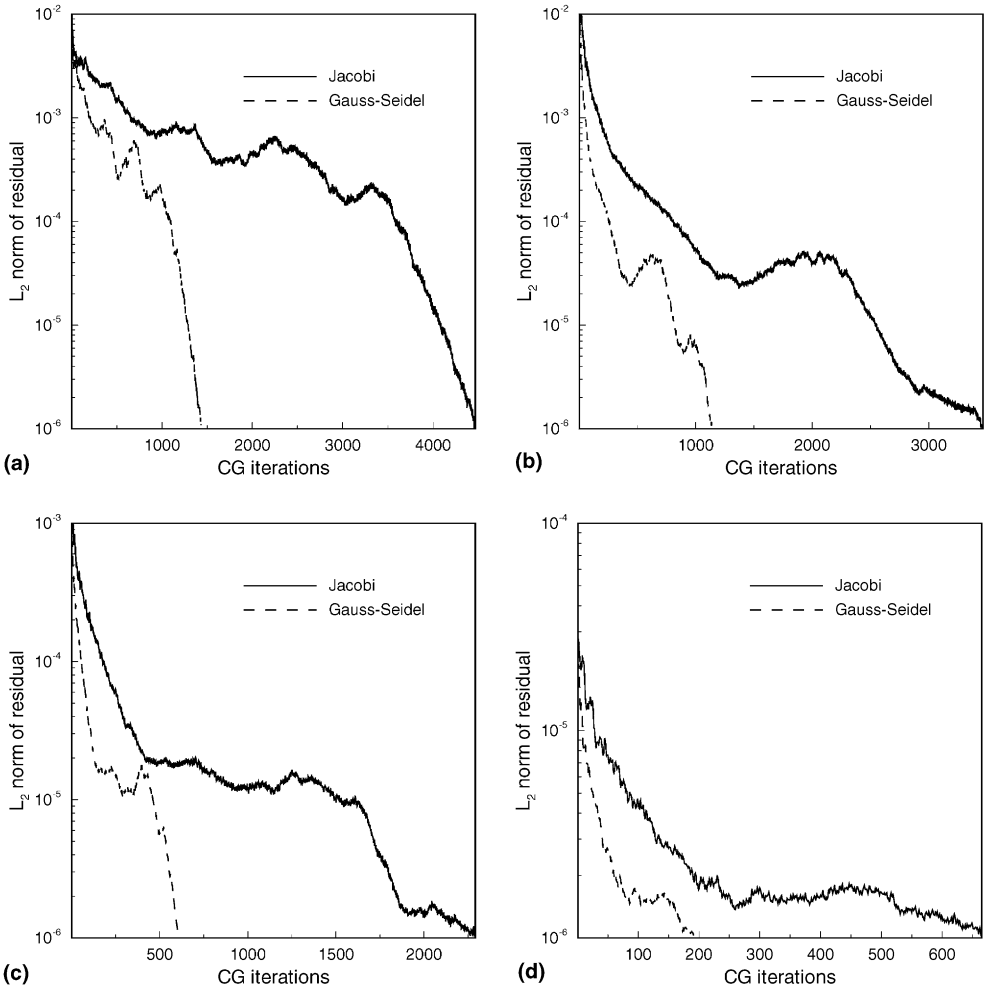

Fig. 11. Convergence history of the conjugate gradient (CG) solver using a Jacobi and a Gauss–Seidel preconditioner: (a)–(d) corresponding to Newton iterations 1–4, for an 11th order modal expansion and flow conditions of $Re = 800$ in the channel.

not the case for the Jacobi preconditioner. For three-dimensional problems the cost of applying a Gauss–Seidel preconditioner might be high in terms of computer memory. Similar convergence rates and accuracy were observed for the velocity gradient formulation, although at higher CPU solve times due to having additional degrees of freedom.

3.3.3. Flow past a circular cylinder at low Reynolds number

We next consider the two-dimensional flow of an incompressible fluid past a circular cylinder. The Reynolds numbers considered here are 20 and 40, for which a steady-state solution exists. The cylinder is of unit diameter and is placed in the finite region $\bar{\Omega} = [-15.5, 30.5] \times [-20.5, 20.5]$. The center of the cylinder lies at $(x, y) = (0, 0)$, so that the inflow boundary is located 15.5 cylinder diameters in front of the center of the cylinder and the outflow boundary 30.5 cylinder diameters downstream of the center of the cylinder. The top and bottom boundaries are located each 20.5 cylinder diameters above and below the center of the cylinder. The Reynolds number is based on the free-stream velocity and cylinder diameter.

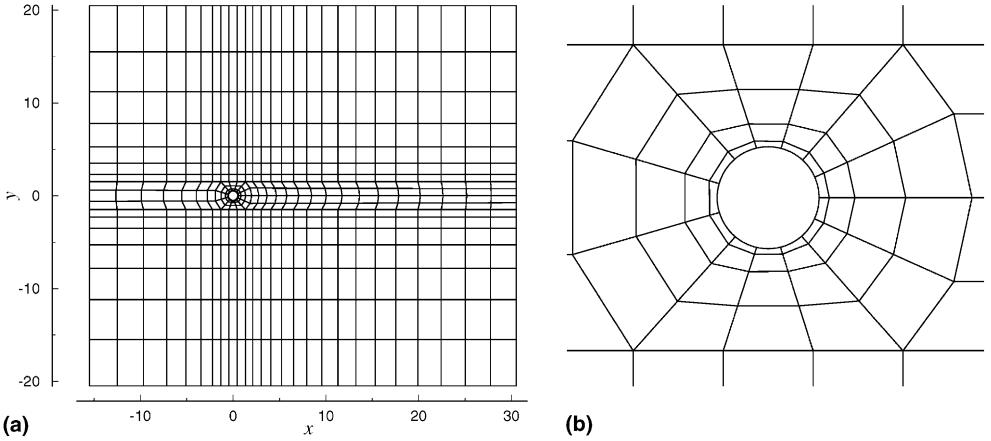

Fig. 12. Computational domain and mesh for flow past a circular cylinder: (a) connected model, $\bar{\Omega}^h$; (b) close-up view of the geometric discretization around the circular cylinder.

Having considered a large computational domain allows us to impose free-stream boundary conditions at the top and bottom of the domain without noticeably affecting the solution. The boundary conditions include a specified value of 1.0 for the x-component of velocity at the inflow, top, and bottom boundaries, i.e., the free-stream velocity u_∞ is specified to be unity. At these boundaries the y-component of velocity is set to zero. The outflow boundary conditions are imposed in a weak sense through the least-squares functional.

The connected model, $\bar{\Omega}^h$, consists of 501 finite elements and is shown in Fig. 12, where a close-up view of the geometric discretization around the circular cylinder is also shown. In the previous examples a subparametric formulation using a linear basis for the mapping, $\bar{\Omega}_e \rightleftarrows \hat{\Omega}_e$, was sufficient to exactly represent the straight-sided geometries. In order to accurately represent the circular surface, we implement an isoparametric formulation; i.e., we use the same expansion order for the element degrees of freedom and for the mapping, $\bar{\Omega}_e \rightleftarrows \hat{\Omega}_e$.

We use the two-dimensional incompressible Navier–Stokes equations in the vorticity based first-order form and a sixth-order nodal expansions in each element, resulting in a discrete model with a total of 73,344 degrees of freedom. We note that, for large two-dimensional or three-dimensional computations, storage of the assembled system of equations in banded or in compressed sparse row/column format may become prohibitively expensive in terms of computer memory. We therefore have to resort to matrix-free techniques, also known as element-by-element solution algorithms, and implement a matrix-free version of the conjugate gradient method with a Jacobi preconditioner. The Gauss–Seidel preconditioner cannot be applied in a matrix-free setting, as it requires storage of the lower and upper parts of the assembled system of equations to perform the preconditioning step. It is necessary to emphasize that the matrix-free conjugate gradient algorithm with a Jacobi preconditioner does not require the assembly of a global matrix, not even an element matrix, which leads to tremendous savings in computer memory; and if implemented properly, considerable solve time speed-ups.

At each Newton step the (SPD) linear system of equations is solved using the matrix-free conjugate gradient algorithm with a Jacobi preconditioner. Convergence of the conjugate gradient method was declared when the norm of the residual was less than 10^{-6}. Nonlinear convergence was declared when the relative norm of the residual in velocities between two consecutive iterations was less than 10^{-4}, which required six Newton iterations. The L_2 least-squares functional remained below 10^{-6} for the flow conditions considered.

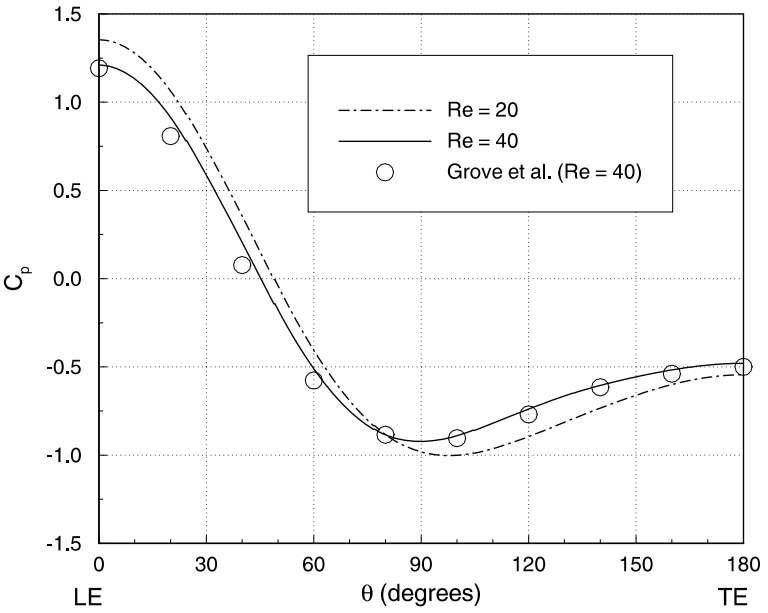

Fig. 13. Flow past a circular cylinder at $Re = 20$ and 40: computed pressure coefficient distributions along the cylinder surface. Comparison with experimental measurements of Grove et al. [19] for the case $Re = 40$.

Fig. 13 shows the computed surface pressure coefficient distributions along the cylinder surface for $Re = 20$ and 40, together with experimental measurements of Grove et al. [19] for the case $Re = 40$. We observe that the simulation result is in good agreement with the experimental measurements. The computed drag coefficients for flow conditions of $Re = 20$ and 40 were $C_D = 2.0862$ and 1.5537, respectively. Good agreement is found between the computed drag coefficients and the experimental mean curve of Tritton [28], where the corresponding values are $C_D = 2.05$ and 1.56.

Fig. 14 shows computed pressure contours and streamlines in the wake region for $Re = 20$ and 40. The predicted wake extends 1.86 and 4.55 cylinder radii measured from the back of the cylinder, respectively.

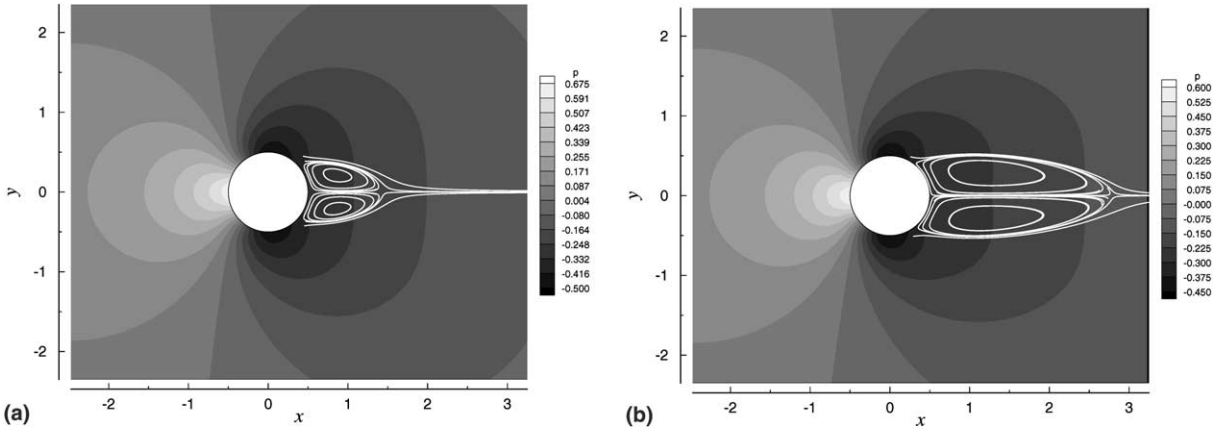

Fig. 14. Flow past a circular cylinder at (a) $Re = 20$ and (b) 40: pressure contours and streamlines in the wake region.

The values for the wake lengths are in good agreement with the numerical solution of Dennis and Chang [29], whose computed wake lengths for $Re = 20$ and 40 were reported as 1.88 and 4.69 cylinder radii, respectively. Better agreement for the case $Re = 40$ is found with the numerical solution of Kawaguti and Jain [30], who reported a computed wake length of 4.50 cylinder radii. Like in the previous example, similar accuracy was observed for the velocity gradient formulation, although at higher CPU solve times due to having additional degrees of freedom.

3.3.4. Lid-driven cavity flow

Next, we consider the three-dimensional flow of an incompressible fluid bounded in a cubic enclosure, $\bar{\Omega} = [0,1] \times [0,1] \times [0,1]$, where the flow is driven by the translation of the top boundary. The connected model, $\bar{\Omega}^h = [0,1] \times [0,1] \times [0,0.5]$, using $6 \times 6 \times 3$ brick finite elements, $\bar{\Omega}_e$, is shown in Fig. 15. It has been established that, up to $Re = 3200$, the flow is symmetric about the plane $z = 0.5$ [31,20]. We therefore model only half the domain.

The Reynolds numbers considered here are 100 and 400, for which it has been well established that a steady-state solution exists. We perform the analysis using the three-dimensional incompressible Navier–Stokes equations in the vorticity based first-order form, for which there are a total of seven primary variables: three velocity components, pressure, and three vorticity components. The boundary conditions are as follows: $u = v = w = 0$ on all solid walls, $p = 0$ at a point, $w = \omega_x = \omega_y = 0$ on the symmetry plane ($z = 0.5$), and $u = u^s(x,z)$, $v = w = 0$ on the top driven surface ($y = 1.0$). On the driven surface we specify a hyperbolic tangent u-velocity distribution: $u^s = g(x)\,g(z)$, where

$$g(s) = \begin{cases} \tanh(\beta s) & 0 \leqslant s \leqslant 0.5, \\ -\tanh(\beta(s-1)) & 0.5 < s \leqslant 1.0 \end{cases}$$

with $\beta > 0$. Here we take $\beta = 50$, which gives a smooth but at the same time sharp transition from $u = 0.0$ to $u = 1.0$ near the walls of the driven surface.

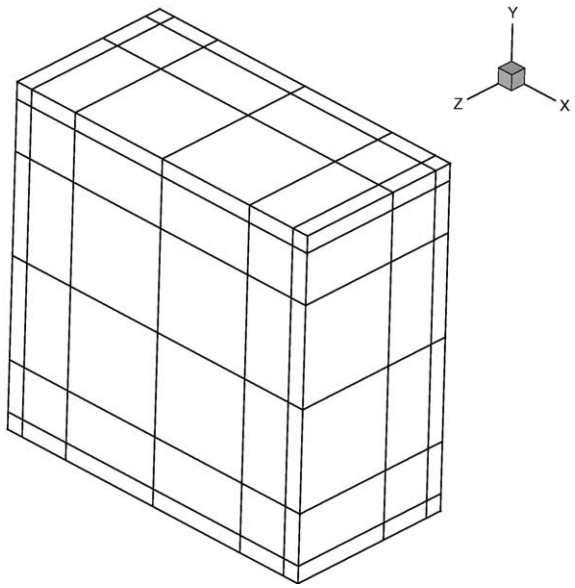

Fig. 15. Computational domain and mesh for the three-dimensional lid-driven cavity problem. Due to symmetry about the plane $z = 0.5$, only half the domain is modeled.

We use a fifth-order nodal expansion in each element, resulting in a discrete model with a total of 107,632 degrees of freedom. The velocity gradient based first-order system was not considered in this study for the solution of three-dimensional flow conditions, as it is significantly more expensive than the vorticity based first-order system. For the discretization considered here, the resulting velocity gradient based discrete model would have a total of 199,888 degrees of freedom. Which, based on results from the two-dimensional numerical examples, would yield equally accurate results when compared to the vorticity-based formulation.

At each Newton step the (SPD) linear system of equations is solved using the matrix-free conjugate gradient algorithm with a Jacobi preconditioner. Convergence of the conjugate gradient method was declared when the norm of the residual was less than 10^{-6}. Nonlinear convergence was declared when the

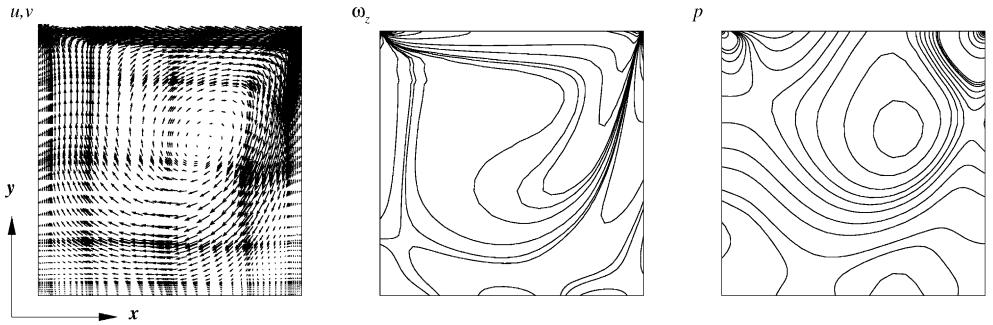

Fig. 16. Velocity vectors, vorticity, and pressure contours on plane $z = 0.5$ for $Re = 400$.

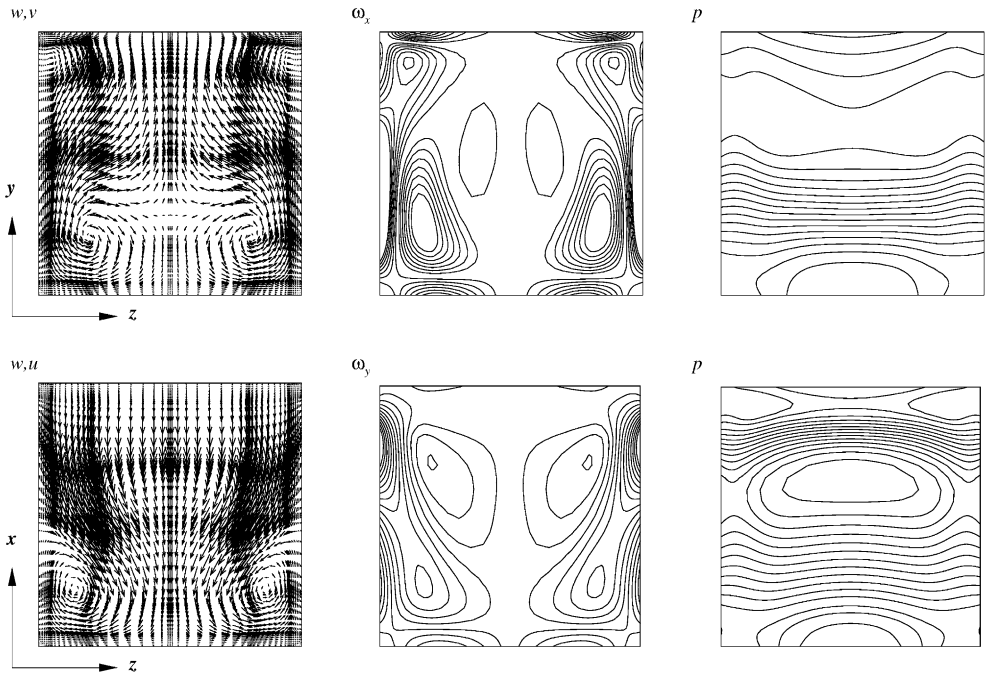

Fig. 17. Velocity vectors, vorticity, and pressure contours on planes $x = 0.5$ and $y = 0.5$ for $Re = 400$.

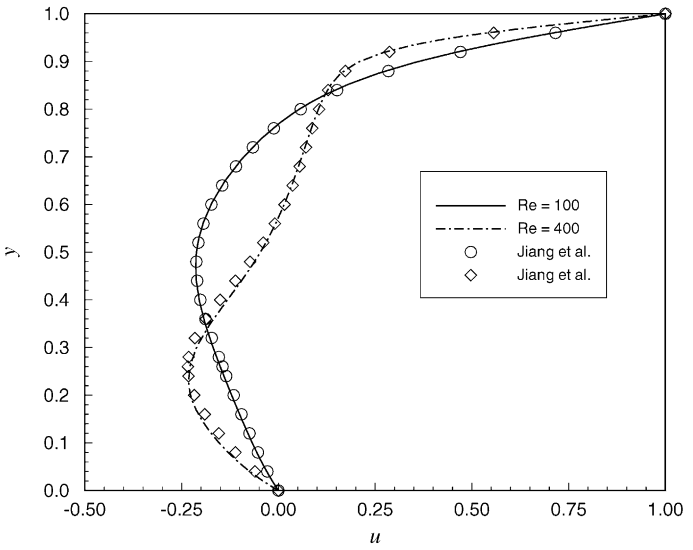

Fig. 18. Profiles of u-velocity along the vertical mid-line of the plane $z = 0.5$. Comparison with tabulated values from the published results of Jiang et al. [20].

relative norm of the residual in velocities was less than 10^{-4}, which typically required six Newton iterations. The analysis starts with $Re = 100$ and steps to $Re = 400$ using a solution continuation technique with increments of $Re = 100$. The L_2 least-squares functional remained below 10^{-3} for the flow conditions considered.

Fig. 16 shows velocity vectors, vorticity contours , and pressure contours on the plane $z = 0.5$ for $Re = 400$. On this plane, we see the primary re-circulation region which looks similar to the well documented two-dimensional solution. Fig. 17 show the solution on the planes $x = 0.5$ and $y = 0.5$. We see a pair of vortices at the bottom wall of the plane $x = 0.5$ and a weak pair of vortices near the top wall. On the plane $y = 0.5$ we see vortices on the side-wall of the cavity. Fig. 18 shows u-velocity profiles along the vertical mid-line of the plane $z = 0.5$, our results are in good agreement with tabulated data from published results of Jiang et al. [20]. Jiang and co-workers used a least-squares finite element formulation with an almost uniform $50 \times 52 \times 25$ mesh with tri-linear elements and *reduced integration*, i.e., one point quadrature.

4. The low-speed compressible Navier–Stokes equations

We consider the solution of the Navier–Stokes equations governing compressible flow. Since we are interested in low-speed flows, the pressure distribution is rather uniform. We consider pressure as composed of small variations p' and a uniform background pressure $\bar{p}$, i.e., $p = \bar{p} + p'$, where $\bar{p} = \rho_\infty R T_\infty$. The background pressure can be dropped from the spatial derivatives and the pressure variation is non-dimensionalized by a reference kinetic energy $\rho_\infty U_\infty^2$. The governing equations in dimensionless form can be written as

Find the density $\rho(\mathbf{x})$, velocity $\mathbf{u}(\mathbf{x})$, pressure $p'(\mathbf{x})$, and temperature $T(\mathbf{x})$ such that

$$(\mathbf{u}\cdot\nabla)\rho + \rho(\nabla\cdot\mathbf{u}) = 0 \quad \text{in } \Omega, \tag{39}$$

$$\rho(\mathbf{u}\cdot\nabla)\mathbf{u} + \nabla p' - \frac{1}{Re}\nabla\cdot\left[(\nabla\mathbf{u}) + (\nabla\mathbf{u})^{\mathrm{T}}\right] + \frac{2}{3}\frac{1}{Re}\nabla(\nabla\cdot\mathbf{u}) = \mathbf{f} + \frac{1}{2\epsilon Fr}\rho(-\hat{\mathbf{k}}) \quad \text{in } \Omega, \tag{40}$$

$$\rho(\mathbf{u}\cdot\nabla)T-\frac{1}{Pe}\nabla^2T-(\gamma-1)M^2(\mathbf{u}\cdot\nabla)p'=\frac{(\gamma-1)M^2}{Re}\Phi-\frac{(\gamma-1)M^2}{2\epsilon Fr}\rho\hat{\mathbf{k}}\cdot\mathbf{u}\quad\text{in }\Omega, \tag{41}$$

$$1+\gamma M^2p'=\rho T\quad\text{in }\Omega, \tag{42}$$

where M is the Mach number, Fr is the Froude number, Pr is the Prandtl number, Re is the Reynolds number, Pe is the Peclet number, γ is the ratio of specific heats, and we assume gravity acts in the $-\hat{\mathbf{k}}$ direction. The temperature difference parameter ϵ is defined as $\epsilon=(T_h-T_c)/(T_h+T_c)$, where T_h and T_c are the specified hot and cold temperatures in a thermal convection problem. We assume appropriate boundary conditions are given and that a unique solution exists.

For low-speed flows ($M<0.3$), the pressure term, the viscous dissipation term, and the buoyancy term in the energy equation (Eq. (41)) become negligible. Furthermore, according to the equation of state (Eq. (42)), the density and temperature become reciprocal. The resulting equations describe *anaelastic* flow conditions, where acoustic phenomena is removed while still allowing for buoyancy and inertial effects of variable density; see [32]. Yu et al. [21] used vorticity, dilatation, and heat flux to reduce the low-speed compressible Navier–Stokes equations to a first-order system. Here we present a velocity gradient/heat flux first-order system.

4.1. The velocity gradient/heat flux based first-order system

Introducing the gradient of the velocity vector field and temperature field as independent variables, the low-speed compressible Navier–Stokes first-order system equivalent in dimensionless form can be written as:

Find the density $\rho(\mathbf{x})$, velocity $\mathbf{u}(\mathbf{x})$, pressure $p'(\mathbf{x})$, velocity gradients $\underline{\mathbf{U}}(\mathbf{x})$, temperature $T(\mathbf{x})$, and heat flux $\mathbf{q}(\mathbf{x})$ such that

$$(\mathbf{u}\cdot\nabla)\rho+\rho(\mathrm{tr}\,\underline{\mathbf{U}})=0\quad\text{in }\Omega, \tag{43}$$

$$\rho(\mathbf{u}\cdot\underline{\mathbf{U}})^{\mathrm{T}}+\nabla p'-\frac{1}{Re}(\nabla\cdot\underline{\mathbf{U}})^{\mathrm{T}}-\frac{1}{3}\frac{1}{Re}\nabla(\mathrm{tr}\,\underline{\mathbf{U}})=\mathbf{f}+\frac{1}{2\epsilon Fr}\rho(-\hat{\mathbf{k}})\quad\text{in }\Omega, \tag{44}$$

$$\underline{\mathbf{U}}-\nabla(\mathbf{u})^{\mathrm{T}}=\underline{\mathbf{0}}\quad\text{in }\Omega, \tag{45}$$

$$\nabla\times\underline{\mathbf{U}}=\underline{\mathbf{0}}\quad\text{in }\Omega, \tag{46}$$

$$\rho(\mathbf{u}\cdot\nabla)T+\nabla\cdot\mathbf{q}=0\quad\text{in }\Omega, \tag{47}$$

$$\mathbf{q}+\frac{1}{Pe}\nabla T=\mathbf{0}\quad\text{in }\Omega, \tag{48}$$

$$\nabla\times\mathbf{q}=\mathbf{0}\quad\text{in }\Omega, \tag{49}$$

$$\rho=\frac{1}{T}\quad\text{in }\Omega. \tag{50}$$

We proceed by using the reciprocal relation between temperature and density to eliminate density from the system of equations. The L_2 least-squares formulation and finite element model proceed in a similar manner as described for the Poisson and incompressible Navier–Stokes equations.

4.2. Numerical example: buoyancy-driven flow inside a square enclosure

We consider two-dimensional, steady, buoyancy-driven gas flow in a square enclosure. The square enclosure is taken to be the unit square, $\bar{\Omega} = [0,1] \times [0,1]$. The connected model $\bar{\Omega}^h$ using 6×6 quadrilateral finite elements, $\bar{\Omega}_e$, is shown in Fig. 19. Boundary conditions are also shown in Fig. 19 and consist of two insulated horizontal walls and two vertical walls at different temperatures, T_h and T_c.

Flow features depend on the Rayleigh number, Froude number, aspect ratio of the enclosure, and the temperature difference parameter ϵ. The Rayleigh number and the Reynolds number are related through $Re = (RaFr/Pr)^{1/2}$. Here we consider Rayleigh numbers 10^3, 10^4, 10^5 with $\epsilon = 0.6$, i.e., $T_h/T_c = 4$. For the Rayleigh numbers considered here, a fifth-order *nodal* expansion in each element is sufficient. The discrete model is linearized using Newton's method and at each Newton step the resulting (SPD) algebraic problem solved using the conjugate gradient method with a symmetric Gauss–Seidel preconditioner. Convergence of the conjugate gradient method was declared when the norm of the residual was less than 10^{-7}. Nonlinear convergence was declared when the relative norm of the solution vector was less than 10^{-4}, which typically required four Newton iterations. The L_2 least-squares functional remained below 10^{-5} for the three flow conditions considered.

Fig. 20 shows streamlines of the flow field and velocity profiles along the horizontal and vertical mid-lines of the the enclosure for the three Rayleigh numbers. The open circles in Fig. 20 are tabulated data from the benchmark solution of Yu et al. [21] for the same flow conditions. We see excellent agreement between our solution and the benchmark solution. Yu and co-workers used a least-squares finite element formulation, and introduced vorticity, dilatation, and heat flux to reduce the low-speed compressible Navier–Stokes equations to a first-order system. They used bi-quadratic elements and *reduced integration* with grid systems ranging from 33×33 to 129×129 elements. The first-order system used by Yu and co-workers was also implemented and found to give equally accurate results at significantly lower CPU solve times, having only vorticity and heat fluxes as additional degrees of freedom.

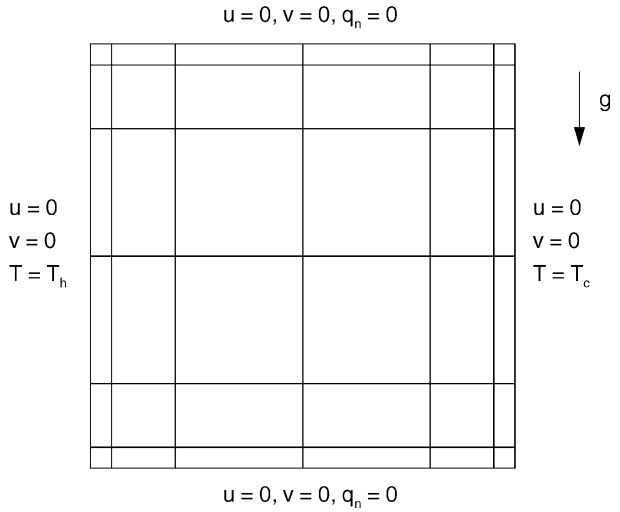

Fig. 19. Geometry, mesh, and boundary conditions for buoyancy-driven gas flow inside a square enclosure.

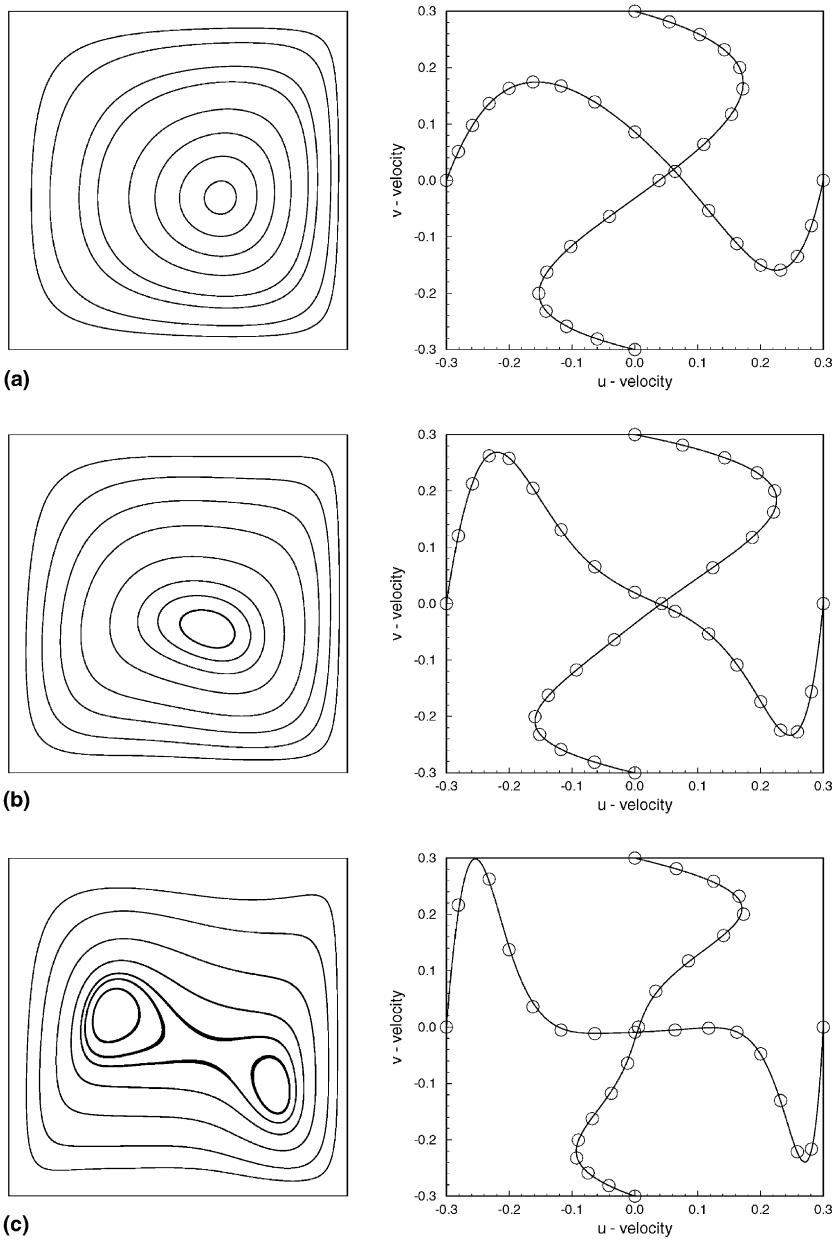

Fig. 20. Streamlines of the flow field and velocity profiles along the horizontal and vertical mid-lines of the enclosure for: (a) $Ra = 10^3$, (b) $Ra = 10^4$, and (c) $Ra = 10^5$. (—) fifth-order nodal expansion, (○) Yu et al. [21].

5. Concluding remarks

In this paper we presented the formulation, validation, and application of spectral/*hp* least-squares finite element methods for the Navier–Stokes equations. Spectral convergence of the L_2 least-squares functional and L_2 error norms were verified using smooth solutions to the Poisson equation and the Kovasznay flow

solution to the incompressible Navier–Stokes equations. For practical implementation of the least-squares finite element formulation, the Navier–Stokes equations were reduced to an equivalent first-order system by introducing the vorticity vector or the gradient of the velocity vector field as additional primary variables. Outflow boundary conditions were imposed in a weak sense through the least-squares functional. Numerical results for incompressible flow over a backward-facing step, steady flow past a circular cylinder, three-dimensional lid-driven cavity flow, and low-speed compressible buoyant flow inside a square enclosure were presented and found to be in excellent agreement with benchmark solutions.

Predominantly low order nodal expansions have been used to develop discrete finite element models of the Navier–Stokes equations by least-squares finite element formulations. Low order nodal expansions have been found to lock for non-equivalent formulations and reduced integration is needed to yield acceptable numerical results. In our experience with reduced integration, we have found that the resulting assembled matrix is nearly singular. Furthermore, the numerical solution may not be smooth at the nodes and post-processing is needed to recover nodal values from the reduced integration points.

In this paper we made use of full integration throughout, with no post-processing of the numerical solution. The quality of the numerical solution was judged by the value of the L_2 least-squares functional, which was shown to decay exponentially fast as the expansion order of the element nodal/modal basis is increased. With regard to computational cost and efficiency, the assembled system of equations are solved in a fully coupled manner by the preconditioned conjugate gradient method using a Gauss–Seidel or Jacobi preconditioner. For large two-dimensional or three-dimensional problems a conjugate gradient matrix-free algorithm with a Jacobi preconditioner is used. The element-by-element nature of the algorithm naturally allows for its parallelization. The vorticity based first-order systems were found to give equally accurate results when compared to the velocity gradient based first-order systems, at significantly lower CPU solve times due to having introduced fewer additional degrees of freedom. We may thus conclude that, for the incompressible and low-speed compressible Navier–Stokes equations, the vorticity based formulations are the most efficient.

Extension of the formulation to the non-stationary Navier–Stokes equations [33] and viscous compressible flows for subsonic/transonic flow conditions are the subjects of forthcoming papers.

Acknowledgements

The support of this research by the Computational Mathematics Program of the Air Force Office of Scientific Research is gratefully acknowledged. The first author also acknowledges the support of this work through a Computational Science and Engineering Program Graduate Fellowship from Texas A&M University. The authors are grateful to Dr. Richard Ewing, Vice President for Research, for his support and encouragement of this research.

References

[1] G.E. Karniadakis, S.J. Sherwin, Spectral/*hp* Element Methods forCFD, Oxford University Press, Oxford, 1999.
[2] J.N. Reddy, Energy Principles and Variational Methods in Applied Mechanics, second ed., Wiley, New York, 2002.
[3] V. Girault, P. Raviart, Finite Element Methods for Navier–Stokes Equations, Springer, Berlin, 1986.
[4] F. Brezzi, J. Douglas, Stabilized mixed methods for the Stokes problem, Numer. Math. 53 (1988) 225.
[5] L. Franca, R. Stenberg, Error analysis of some Galerkin least-squares methods for the elasticity equations, SIAM J. Numer. Anal. 28 (1991) 1680.
[6] B.N. Jiang, The Least-Squares Finite Element Method, Springer, Berlin, 1998.
[7] P.B. Bochev, M.D. Gunzburger, Finite element methods of least-squares type, SIAM Rev. 40 (1998) 789.
[8] S. Agmon, A. Douglis, L. Nirenberg, Estimates near the boundary for solutions of elliptic partial differential equations satisfying general boundary conditions II, Commun. Pure Appl. Math. 17 (1964) 35.

[9] Z. Cai, T.A. Manteuffel, S.F. McCormick, First-order system least-squares for the Stokes equations, with applications to linear elasticity, SIAM J. Numer. Anal. 34 (1997) 1727.
[10] P.B. Bochev, Analysis of least-squares finite element methods for the Navier–Stokes equations, SIAM J. Numer. Anal. 34 (1997) 1817.
[11] B.N. Jiang, A least-squares finite element method for incompressible Navier–Stokes problems, Int. J. Numer. Methods Fluids 14 (1992) 843.
[12] L.Q. Tang, T.H. Tsang, Temporal, spatial and thermal features of 3-D Rayleigh–Benard convection by a least-squares finite element method, Comput. Methods Appl. Mech. Eng. 140 (1997) 201.
[13] P.B. Bochev, Z. Cai, T.A. Manteuffel, S.F. McCormick, Analysis of velocity-flux least-squares principles for the Navier–Stokes equations, Part I, SIAM J. Numer. Anal. 35 (1998) 990.
[14] B.N. Jiang, V. Sonnad, Least-squares solution of incompressible Navier–Stokes equations with the *p*-version of finite elements, Comput. Mech. 15 (1994) 129.
[15] D. Winterscheidt, K.S. Surana, *p*-Version least-squares finite element formulation for two-dimensional incompressible fluid flow, Int. J. Numer. Methods Fluids 18 (1994) 43.
[16] M. Bagheri, K.S. Surana, *p*-Version least-squares finite element formulation for steady-state two-dimensional turbulent flows using the k-ε model of turbulence, Commun. Numer. Meth. Eng. 16 (2000) 97.
[17] T.C. Warburton, S.J. Sherwin, G.E. Karniadakis, Basis functions for triangular and quadrilateral high-order elements, SIAM J. Sci. Comput. 20 (1999) 1671.
[18] D.K. Gartling, A test problem for outflow boundary conditions—flow over a backward-facing step, Int. J. Numer. Methods Fluids 11 (1990) 953.
[19] A.S. Grove, F.H. Shair, E.E. Petersen, A. Acrivos, An experimental investigation of the steady separated flow past a circular cylinder, J. Fluid Mech. 19 (1964) 60.
[20] B.N. Jiang, T.L. Lin, L.A. Povinelli, Large-scale computation of incompressible viscous flow by least-squares finite element method, Comput. Methods Appl. Mech. Eng. 114 (1994) 213.
[21] S.T. Yu, B.N. Jiang, J. Wu, N.S. Liu, A div–curl grad formulation for compressible buoyant flows solved by the least-squares finite element method, Comput. Methods Appl. Mech. Eng. 137 (1996) 59.
[22] J.N. Reddy, An Introduction to the Finite Element Method, second ed., McGraw-Hill, New York, 1993.
[23] J.N. Reddy, An Introduction to Nonlinear Finite Element Analysis, Oxford University Press (2003) (in press).
[24] R.L. Sani, P.M. Gresho, Resume and remarks on the open boundary condition minisymposium, Int. J. Numer. Methods Fluids 18 (1994) 983.
[25] L.S.G. Kovasznay, Laminar flow behind a two-dimensional grid, Proc. Camb. Phil. Soc. 44 (1948) 58.
[26] M.M.J. Proot, M.I. Gerrtisma, Least-squares spectral elements applied to the Stokes problem, J. Comput. Phys. 181 (2002) 454.
[27] Y. Saad, Iterative Methods for Sparse Linear Systems, PWS, 1996.
[28] D.J. Tritton, Experiments on the flow past a circular cylinder at low Reynolds numbers, J. Fluid Mech. 6 (1959) 547.
[29] S.C.R. Dennis, G.Z. Chang, Numerical solutions for steady flow past a circular cylinder at Reynolds numbers up to 100, J. Fluid Mech. 42 (1970) 471.
[30] M. Kawaguti, P. Jain, Numerical study of a viscous fluid past a circular cylinder, J. Phys. Soc. Jpn. 21 (1966) 2055.
[31] J.N. Reddy, Penalty-finite-element analysis of 3-D Navier–Stokes equations, Comput. Methods Appl. Mech. Eng. 35 (1982) 87.
[32] F.S. Sherman, Viscous Flow, McGraw-Hill, New York, 1990.
[33] J.P. Pontaza, J.N. Reddy, Space-time coupled spectral/*hp* least-squares finite element formulation for the incompressible Navier–Stokes equations, J. Comput. Phys. (accepted for publication).